



Bed particle dynamics at entrainment

Matthew J. Witz, Stuart Cameron & Vladimir Nikora

To cite this article: Matthew J. Witz, Stuart Cameron & Vladimir Nikora (2019) Bed particle dynamics at entrainment, Journal of Hydraulic Research, 57:4, 464-474, DOI: [10.1080/00221686.2018.1489898](https://doi.org/10.1080/00221686.2018.1489898)

To link to this article: <https://doi.org/10.1080/00221686.2018.1489898>



© 2018 The Author(s). Published by Informa UK Limited, trading as Taylor & Francis Group



Published online: 28 Aug 2018.



Submit your article to this journal [↗](#)



Article views: 1621



View related articles [↗](#)



View Crossmark data [↗](#)



Citing articles: 1 View citing articles [↗](#)




Research paper

Bed particle dynamics at entrainment

MATTHEW J. WITZ, Honorary Research Fellow, *School of Engineering, University of Aberdeen, Aberdeen AB24 3UE, UK*
Email: mwitz@abdn.ac.uk (author for correspondence)

STUART CAMERON, Research Fellow, *School of Engineering, University of Aberdeen, Aberdeen AB24 3UE, UK*
Email: s.cameron@abdn.ac.uk

VLADIMIR NIKORA  (IAHR Member), Professor, *School of Engineering, University of Aberdeen, Aberdeen AB24 3UE, UK*
Email: v.nikora@abdn.ac.uk

ABSTRACT

The paper reports a high-resolution experimental study focused on statistical properties of particle trajectories starting with detachment from the bed. This local range of particle motion can either be considered to start from a collision with the bed of an already mobile particle, or from the entrainment of a previously immobile particle. Both approaches are investigated and compared based on the particle diffusion concept. From the point of entrainment, local particle diffusion in all three coordinate directions displays an exponent significantly greater than that of ballistic diffusion. In contrast, particle motion after collision with the bed demonstrates ballistic diffusion in all three coordinate directions. The results highlight clear differences between the diffusion of an already mobile particle and one starting from a position of rest. These differences are attributed to variations in physical mechanisms acting at the initial phase of particle motion after detachment from the bed.

Keywords: Bedload; entrainment; particle diffusion; particle velocity; sediment transport; turbulence–sediment interactions

1 Introduction

Bed particle motion can be classified into three distinct types: sliding, rolling and saltating. A sliding particle moves with one of its sides in almost constant contact with the bed, typically occurring for large angular particles with a flat face (e.g. Drake, Shreve, Dietrich, Whiting, & Leopold, 1988). Rolling particles undergo rotational motion and are in regular contact with the bed. Due to the similarity of the motion in three-dimensional space, rolling and sliding can be difficult to distinguish; as such they are often treated as a single mode of motion (e.g. Nikora, Heald, Goring, & McEwan, 2001). In contrast, saltation describes motion that consists of a series of jumps separated by brief contact with the bed. The type of motion experienced by a particle depends upon its shape and size, the near-bed flow velocity and, to a lesser extent, the underlying bed arrangement. The motion of a single particle may change between modes as it travels.

Nikora et al. (2001) and Nikora, Habersack, Huber, and McEwan (2002) suggested that bed particle motion, regardless of the type, can be divided into three scale ranges: local, intermediate

and global. The global scale considers the complete and ongoing motion of a particle, including numerous motions, interactions with the bed, and rest periods (during which the particle does not move). As a subset of the global scale, the intermediate scale accounts for the motion of a particle between two rest periods; this may include several interactions with the bed and changes of particle motion direction. For saltating particles (considered here), the local scale is the motion between two successive contacts with the bed. This work will focus on this local range, which is the least explored range of particle motion, as highlighted by Campagnol, Radice, Ballio, and Nikora (2015), who proposed a general conceptual picture for this range (fig. 13 in their paper).

The motion of bed load particles depends on the combination of several parameters reflecting its stochastic nature: the waiting time between motions, the time in motion and the jump length (e.g. Bialik, Nikora, Karpiński, & Rowiński, 2015). The spread of particles due to the stochastic nature of bed load transport is known as bed particle diffusion (e.g. Nikora et al., 2002). A key diffusion characteristic is the change in time of the second central moment of particle position:

Received 14 April 2017; accepted 14 May 2018/Open for discussion until 29 February 2020.

$$\overline{x_j^2} \propto t^{2\gamma_j} \quad (1)$$

where $\overline{x_j^2}$ can be estimated as:

$$\overline{x_j^2} = \frac{1}{N} \sum_N [x_j(t) - \overline{x_j}(t)]^2 \quad (2)$$

In the equations above, γ is the diffusion exponent, x_j is the particle position (where j determines the direction), N is the number of particle trajectories being considered (assumed to be large), t is the time from entrainment, and the over-bar indicates an average over N entrainments. In general, the diffusion can be classified into different regimes: normal (or Fickian) ($\gamma_x \equiv \gamma_y \equiv \gamma_z \equiv 0.5$), ballistic ($\gamma_x \equiv \gamma_y \equiv \gamma_z \equiv 1$), superdiffusive ($(\gamma_x, \gamma_y, \gamma_z) > 0.5$) and subdiffusive ($(\gamma_x, \gamma_y, \gamma_z) < 0.5$) (e.g. Nikora et al., 2002). Additionally, diffusion with $\gamma_i \neq 0.5$ is referred to as anomalous, where the subscript i stands for x , y or z .

Nikora et al. (2002) hypothesized that in the horizontal (x, y) plane the diffusion regimes may depend on the particle motion scale; global scale diffusion is likely to be subdiffusive, intermediate scale can be subdiffusive, normal or superdiffusive, and local scale is ballistic. Subdiffusive behaviour in the global range of particle motion was suggested by Nikora et al. (2002) based on the re-analysis of the data from Drake et al. (1988). This suggestion was supported by numerical simulations by Bialik, Nikora, and Rowiński (2012). In line with the suggestion by Nikora et al. (2002), follow-up studies have shown that the intermediate range can be governed by subdiffusion (Fan, Singh, Fofoula-Georgiou, & Wu, 2013), normal diffusion (e.g. Fan et al., 2013; Furbish, Ball, & Schmeeckle, 2012) or superdiffusion (Bialik et al., 2012; Fan et al., 2013; Martin, Jerolmack, & Schumer, 2012). However, the validity of superdiffusion in the intermediate range has been questioned, with the suggestion that superdiffusion apparent in second order central moment plots may be because of correlated random walks due to inherent periodicities in the particle motions, as opposed to being true anomalous diffusion (Furbish et al., 2012; Roseberry, Schmeeckle, & Furbish, 2012).

In the case of a saltating particle, a general local particle motion starts and finishes with an impact with the bed. However, this is not the case for all local particle motions. Specifically, it is not the case when the particle is entrained from a position of rest (i.e. for the first local motion in each intermediate range of motion). Due to the different mechanisms involved, the resulting diffusion from a bed impact and from entrainment can be expected to be distinct. When ballistic diffusion was suggested for the local scale range by Nikora et al. (2002), the data were not available to support this. However, it has since been shown to be the case in several studies (Bialik et al., 2012; Furbish et al., 2012; Roseberry et al., 2012). The presence of ballistic diffusion in the local range has been confirmed by studies that have either: (1) taken a particle collision with the bed as the start of the local range (e.g. Bialik et al., 2012); or (2) had insufficient

resolution to track the initial motion of the particle (Roseberry et al., 2012). Recent work has shown that diffusion from entrainment exhibits diffusion exponents larger than that of ballistic motion (Bialik et al., 2015, 2012; Campagnol et al., 2015). By undertaking numerical simulations, Bialik et al. (2012) considered the effect of diffusion from both bed impacts and entrainment and found that diffusion from entrainment had exponents significantly greater than those of diffusion from bed impacts (ballistic diffusion). However, their work considered entrainment from a fully exposed position that is unlikely to exist in reality, and it took the point of entrainment as the time at which the particle moved downstream by a particle diameter, resulting in a loss of information about its initial motion. A more recent numerical study by Bialik et al. (2015) modelled particle motion from placement/release on the bed; however, the results presented either include waiting time prior to entrainment, or represent placement in an exposed position where entrainment occurs immediately upon release. In addition, as with many simulations of complex phenomena, models and assumptions are required (e.g. the force components responsible for entrainment and the mechanics of particle collisions), which may not represent the reality in full. Nevertheless, the laboratory experiments of Ballio, Campagnol, Nikora, and Radice (2013) also showed that the scaling diffusion exponents for entrained particles are significantly higher compared to those for a random bed contact. Campagnol et al. (2015) provided additional supporting data and proposed a concept for the local scale range that accounts for particle unsteadiness at the entrainment stage. This concept is used in our study as general guidance.

As highlighted above, particle motion within the local scale range is not clearly defined and requires additional study. This paper employs three-dimensional particle tracking in high-precision laboratory experiments to investigate particle motion within the local range for all three coordinate directions. In particular, this work aims to determine the effect of the initial condition on particle motion. The experiments and data analysis techniques are detailed in Section 2, with the resulting particle motions covered in Section 3 (where diffusion from entrainment and a bed collision are considered separately). The findings are drawn together in the discussion (Section 4).

2 Experiments and data analysis

This section describes the experimental methods, hydraulic scenarios and data analysis techniques.

2.1 Experimental design

Experiments were performed in an 18 m long, 1.18 m wide recirculating open channel flume. The entire bed of the flume was covered with a single layer of glass spheres (16 mm diameter) in a hexagonal close packing arrangement (Fig. 1c). A

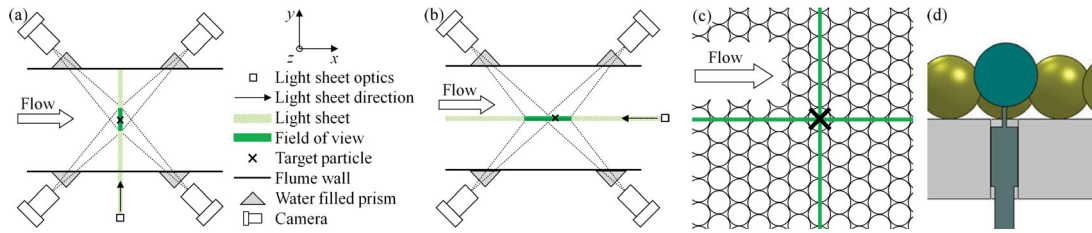


Figure 1 Experimental configurations: (a) TPIV (plan view), (b) SPIV (plan view), (c) particle arrangement (plan view), (d) particle arrangement (side view)

perforated steel plate was attached to the bed of the flume to host the particles, securing a high-precision particle arrangement.

The tracking of particle trajectories utilized part of the data collected during a comprehensive set of experiments on particle entrainment (Witz, 2015). Using a manual device, designed to minimize disturbance to the flow whilst guiding the particle into the bed pocket, a single low density sphere was placed on the bed and then the particle image velocimetry (PIV) system was started and run until 10 s after entrainment. The average time for the particle to entrain was set by altering the protrusion (P) of the particle (the height from the top of the entrainment particle to the top of the surrounding bed particles). The entrainment particle was supported by a metal bar that passed through the bed of the flume (Fig. 1d); the height of the bar was adjusted to achieve the required protrusion. Waiting time is highly sensitive to protrusion, which was set for each flow condition and particle density combination to achieve a mean waiting time of approximately 120 s. PIV recordings were used to track the position of the entrained particle in three dimensions (detailed in Section 2.3). Two different stereoscopic PIV modes were employed to provide flow description at entrainment moments in both planes $y-z$ and $x-z$, corresponding to a transverse stereoscopic configuration (TPIV) and to a streamwise panoramic stereoscopic configuration (SPIV) respectively. The detailed analysis of the flow velocity datasets will be reported elsewhere, while here we use the obtained PIV videos to obtain particle trajectories. Both configurations employ four cameras, each consisting of a Dalsa (Waterloo, Canada) sensor, a Nikon (Tokyo, Japan) lens and a custom manufactured Scheimpflug mount. The Scheimpflug mount allows for lens movement in the horizontal plane along two perpendicular axes and a rotation of $\pm 15^\circ$ between the sensor and the lens to enable the Scheimpflug condition to be satisfied.

TPIV consisted of a light sheet orientated in the transverse vertical ($y-z$) plane with four cameras viewing the same field of view from four different locations (Fig. 1a). The field of view seen by all cameras is approximately 300 mm in the transverse direction and covers the full flow depth; it is located symmetrically about the flume centreline, positioned directly over the protruding particle. The cameras are located at the sides of the flume channel at an angle of approximately 45° to the flume centreline; they view the measurement section through water-filled glass prisms that are attached to the outside of the flume walls. The prisms are employed to reduce the effect of differential

refraction between the air to glass and glass to water interfaces (Prasad, 2000). The light sheet optics are placed outside the channel with the light sheet entering the flume through the glass side wall.

SPIV is a novel set-up combining stereoscopic measurements with an increased field of view (without decreasing spatial resolution). This involves two pairs of cameras with each pair recording a full flow depth 300 mm long window. There is 100 mm overlap between the two windows. This set-up results in a 500 mm long field of view orientated in the streamwise vertical ($x-z$) plane, positioned along the flume centreline directly over the top of the protruding particle (Fig. 1b). The light sheet optics are located 660 mm downstream of the protruding particle. The cameras are positioned in a similar arrangement to that of TPIV.

2.2 Experimental matrix

The desired entrainment rate, protrusion range and particle availability allowed the selection of two densities of entrainment particle. Three submergences (H/d) were considered for each particle density, resulting in a total of six different scenarios, where each condition was a unique combination of submergence and entrainment particle (Table 1). Overall, 50 separate entrainment events were recorded for each scenario (25 using TPIV configuration and 25 using SPIV configuration). In addition, 10 minute PIV recordings were made with a fixed bed (no entrainment) and with zero protrusion to provide background flow conditions.

2.3 Data analysis

Stereoscopic reconstruction algorithms were applied to track the position of the particle in three-dimensional space; these required the particle to be simultaneously tracked in two different camera images, and the mapping function to transform the camera images into real space. The mapping function is found through PIV calibration techniques employing the pinhole camera model (detailed in Witz, 2015). The two downstream cameras were used to track the position of the particle in both PIV set-ups. The tracking ran from the start of the experiment recording until the particle could no longer be seen by both cameras. For SPIV, the tracking ended in one of two ways: (1) the entrained particle moved in the transverse direction such that no

Table 1 Experimental parameters: H is the flow depth from the roughness tops to the water surface, ρ is the entrainment particle density, ρ_w is the water density, d is the entrainment particle diameter, f is PIV sampling frequency, R is bulk Reynolds number ($R = U_b H / \nu$, where U_b is bulk velocity), F is Froude number ($F = U_b / \sqrt{gH}$), and θ_s is Shields number ($\theta_s = u_*^2 / (\Delta g d)$, where u_* is shear velocity (estimated from the total shear stress distribution obtained from PIV data and extrapolated to the roughness tops) and $\Delta = \rho_s / \rho - 1$).

H (mm)	H/d	ρ/ρ_w	P/d	Entrainments	f (Hz)	R	F	u_* (ms ⁻¹)	θ_s
28.6	1.79	1.12	0.160	50	100	1.15×10^4	0.761	0.0395	0.0817
28.6	1.79	1.38	0.484	50	100	1.15×10^4	0.761	0.0395	0.0259
68.8	4.30	1.12	0.114	50	50	3.24×10^4	0.573	0.0403	0.0852
68.8	4.30	1.38	0.416	50	50	3.24×10^4	0.573	0.0403	0.0270
119.3	7.46	1.12	0.098	50	32	6.17×10^4	0.478	0.0407	0.0866
119.3	7.46	1.38	0.394	50	32	6.17×10^4	0.478	0.0407	0.0275

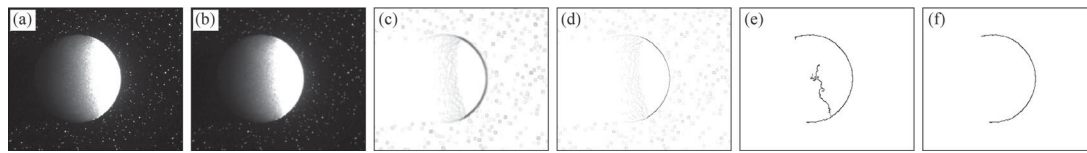


Figure 2 Breakdown of the steps involved in edge detection: (a) original image, (b) Gaussian filter, (c) sobel, (d) non-maximum suppression, (e) length filter, (f) direction filter

part of it remained in the light sheet; or (2) the entrained particle left the viewing window of the cameras. Particle tracking for TPIV was based on the particle blocking the light of the laser sheet from the two downstream cameras (as the particle left the light sheet shortly after entrainment) and ended when the particle left the field of view of the cameras.

Whilst the particle is in the light sheet, a significant intensity gradient occurs at its front edge (the side facing the light source). A technique similar to the Canny edge detector (Canny, 1986, discussed by Cameron, 2006) was employed to make use of this fact and to automate the tracking of the particle. First, a mask was applied to the image to remove the water surface and immobile bed particles from the image. Second, a Gaussian blur was applied to the original image; this is required to reduce the impact of image noise on the edge detection (Fig. 2b). Third, the image was convolved with two Sobel operators G_x and G_y :

$$G_x = \begin{bmatrix} -1 & 0 & 1 \\ -2 & 0 & 2 \\ -1 & 0 & 1 \end{bmatrix}, \quad G_y = \begin{bmatrix} 1 & 2 & 1 \\ 0 & 0 & 0 \\ -1 & -2 & -1 \end{bmatrix} \quad (3)$$

resulting in horizontal (G_x) and vertical (G_y) image gradient fields. The gradient magnitude (G) and direction (θ) are given by:

$$|G| = |G_x| + |G_y| \quad (4)$$

$$\theta = \tan^{-1} \left(\frac{G_y}{G_x} \right) \quad (5)$$

A minimum threshold was applied to the gradient intensities, the value of which is controlled by the user and depends upon

the image conditions, which vary with the protrusion and particle type (Fig. 2c). Fourth, non-maximum suppression (NMS) was used to reduce the thickness of the detected edges. Due to the width of the Sobel operator and the Gaussian blur applied to the image, the detected edges can be several pixels thick. NMS reduces line thickness by suppressing gradients that are not a local maximum in the direction perpendicular to the edge. After applying NMS (Fig. 2d), all detected lines were one pixel thick. Fifth, a length filter was applied to remove short edge detections that were unlikely to be related to the entraining particle (again this parameter was user controlled) (Fig. 2e). Finally, the edges facing the wrong direction (determined from the gradient intensity direction) were removed (Fig. 2f). A circle was fitted to the detected edge using a least squares orthogonal distance fitting method (outlined by Ahn, Rauh, & Warnecke, 2001). The automated tracking worked well while the entrained particle was located in the centre of the light sheet, but once it began to move in the transverse direction the accuracy rapidly deteriorated. Therefore, the particle tracking was checked manually for every entrainment and adjustments made where necessary.

For TPIV, once the particle leaves the light sheet, tracking was performed as follows. First, a mask was applied to remove the water surface and bed from the image. Second, a brightness filter was used to remove all pixels beneath a user controlled level; this ensures that the area of the light sheet blocked by the ball appears completely black on the filtered image. Finally, a spatial search across the image was used to find the pixel that allows the biggest circle to be fitted without intersecting a bright (seeding) particle. This pixel was recorded as the centre of the particle in that frame. The spatial search was initially undertaken on a large grid size, which reduced in size down to a final pass at individual pixel scale. From the point of entrainment the

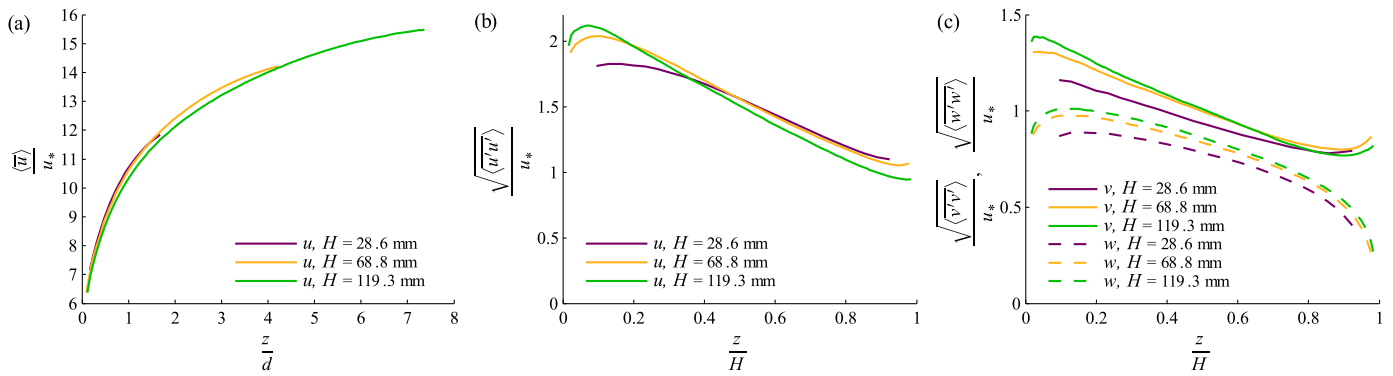


Figure 3 Double-averaged flow properties: (a) streamwise velocity, (b) streamwise turbulence intensity, (c) transverse and vertical turbulence intensities, where $u'_i = u_i - \bar{u}_i$ with overbar denoting time averaging and angular brackets denoting spatial averaging (e.g. Nikora et al., 2007). $z = 0$ corresponds to the centre of the bed particles

tracking was then manually checked and edited as required to improve the accuracy, which was mainly required at time steps where the particle broke the water surface or collided with the bed.

Standard deviation of the error of the estimated particle coordinates was approximately 1 pixel (0.1 mm) for both PIV configurations. Considering that the errors in computing the particle positions from TPIV and SPIV are similar, to achieve more statistically meaningful results, trajectories from both PIV set-ups are considered as a single dataset.

2.4 Background flow conditions

Fixed bed TPIV measurements, with a spatial resolution of 5.9 mm (defined by the PIV transfer function), provide a detailed view of the background flow conditions. Streamwise double-averaged velocities (Nikora et al., 2007) are displayed in Fig. 3a; the double-averaging is performed in time (over the 10 min recording) and space (in the transverse direction, with a width of $\pm H$ from the flume centreline). The double-averaged streamwise velocity profiles for all flow depths collapse well. Throughout the flow depth, double-averaged transverse and vertical

velocities have a magnitude of the same order as the standard errors.

Figure 3b and 3c show the double-averaged turbulence intensities. The data for three submergences collapse well and all components show similar trends; turbulence intensities attain maximum values near the bed and then reduce towards the water surface. At the water surface, there is a rapid decrease in the vertical turbulence intensity, which is compensated for by a gain in the streamwise and transverse turbulence intensities in this region.

3 Results

Throughout this section, the centre of the entrainment particle is located at $x = 0$ and $y = 0$. Since the initial height of the particle depends on protrusion, to allow the results to be compared $z = 0$ corresponds to the centre of the bed particles.

3.1 Trajectories of entrained particles

The trajectories of entrained particles are shown in Fig. 4 for one case ($\rho/\rho_w = 1.12$ and $H = 68.8$ mm). The difference between

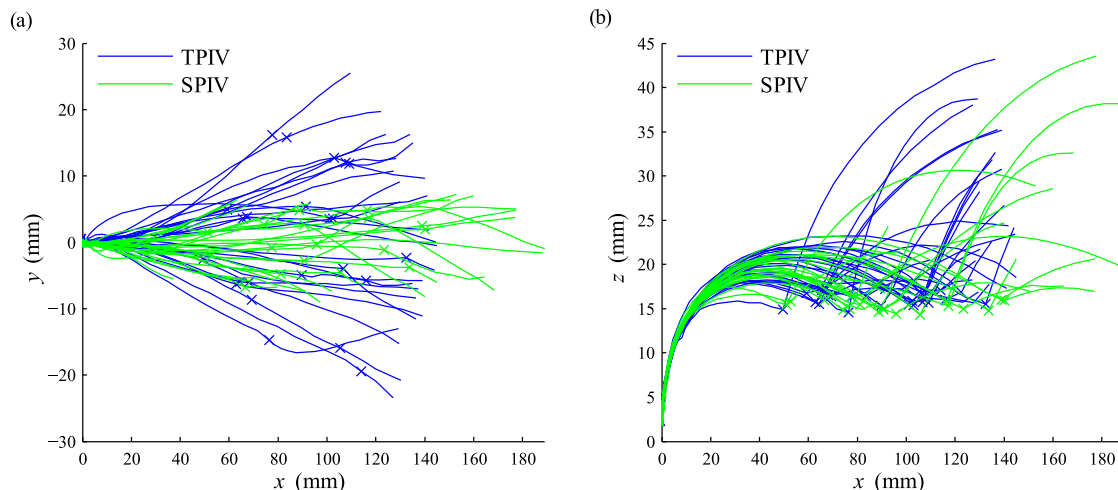


Figure 4 Entrained particle trajectories for $\rho/\rho_w = 1.12$ and $H = 68.8$ mm: (a) horizontal plane, (b) vertical streamwise plane. Collisions with the bed are indicated with crosses

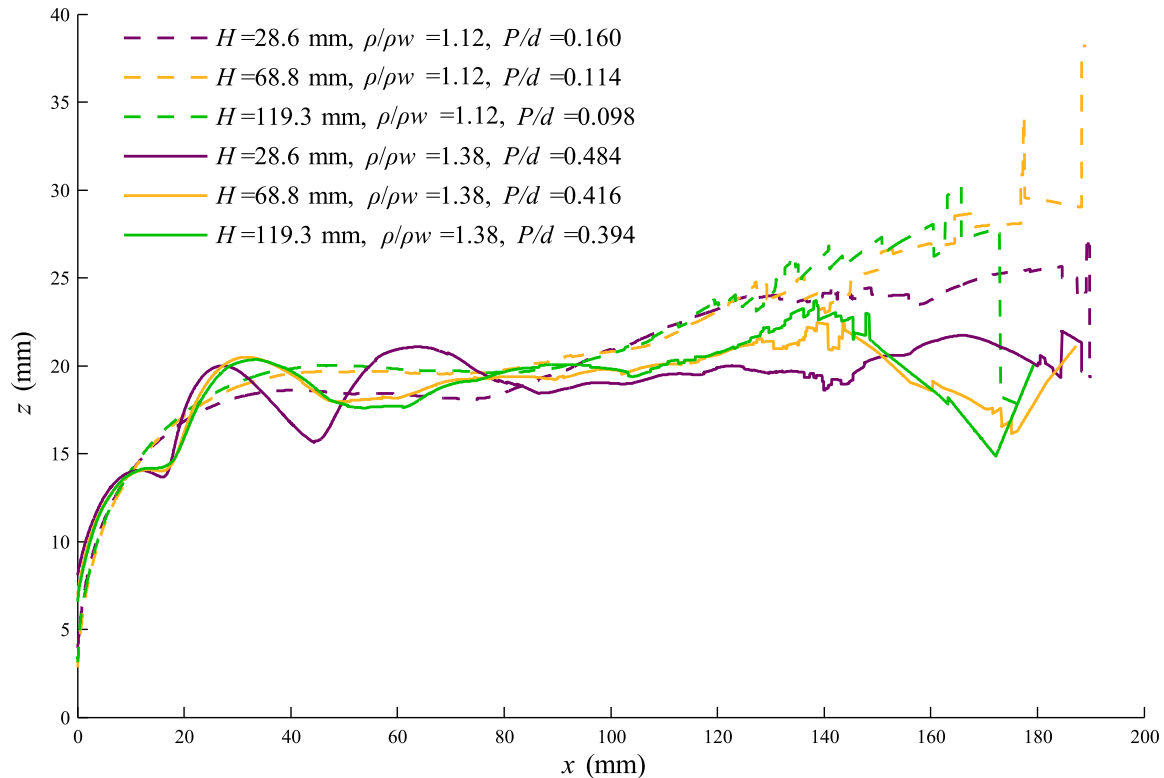


Figure 5 Ensemble-averaged particle trajectories in the streamwise vertical plane

the two PIV set-ups highlights the tracking limitations of the different PIV configurations. For SPIV, the tracking ends when either the particle moves in the transverse direction by $d/2$, or the particle travels approximately 180 mm downstream. Tracking in TPIV terminates when the particle travels a sufficient distance in the horizontal plane to leave the camera images (approximately 145 mm if the particle does not move in the transverse direction). However, almost all entrained particles are tracked for at least 0.8 s after entrainment. Further analysis of the particle trajectories through calculation of diffusion parameters (Section 3.2) is only undertaken up to $t \approx 0.8$ s, therefore reducing the impact of any particle filtering effect on the results presented. Initial motion is governed by the surrounding bed particles; this constraint is removed once the particle has risen out of the bed pocket. However, the time taken for this to occur varies greatly; in the case shown, most particles leave the bed pocket within 0.2 to 0.5 s. The smoothness of the trajectories indicates that once mobile, the particles appear to be unaffected by small scale turbulent velocity fluctuations in the local flow. In fact, significant changes of direction in the transverse orientation typically occur when the saltating particle collides with the bed.

A comparison of the trajectory shapes between different cases is provided in Fig. 5; all entrainments for each case have been ensemble-averaged. For the lighter entrainment particle ($\rho/\rho_w = 1.12$), all cases follow a similar trajectory. The only significant difference is the height of the first jump, with height decreasing as the submergence decreases (and the corresponding protrusion increases). The results are less clear for the higher

density particle ($\rho/\rho_w = 1.38$) because the particles appear to interact with the bed shortly after entraining (approximately 17 mm downstream of its original position).

3.2 Particle diffusion from the point of entrainment

Diffusion times and distances based on the measured trajectories fall into the local scale range (Nikora et al., 2002). The particle motions considered in this section are a distinct subset within the local range where the particle starts from a position of rest (in contrast to a local motion which starts with a bed collision). From the point of entrainment, the displacement (ensemble-averaged), the second-order central moments of the particle position (i.e. diffusion) and the diffusion exponent (local slope of the particle diffusion curve in log-log coordinates) for the streamwise, transverse and vertical directions are displayed in Fig. 6. When considered from the point of entrainment, the particles with two different densities act in markedly different manners. However, all are in the superdiffusive regime and have a significantly greater exponent than for ballistic diffusion, as suggested previously for the local range of motion (Nikora et al., 2001, 2002), where the starting position of each trajectory was a random bed impact, and not a particle entrainment. This difference was considered by Bialik et al. (2012), who found that exponents increased markedly when starting from rest, with $\gamma_x \approx 2.32$ to 2.41 and $\gamma_y \approx 1.84$ to 2.04.

In the streamwise direction, the results of the two particle densities appear to follow different trends. The higher density

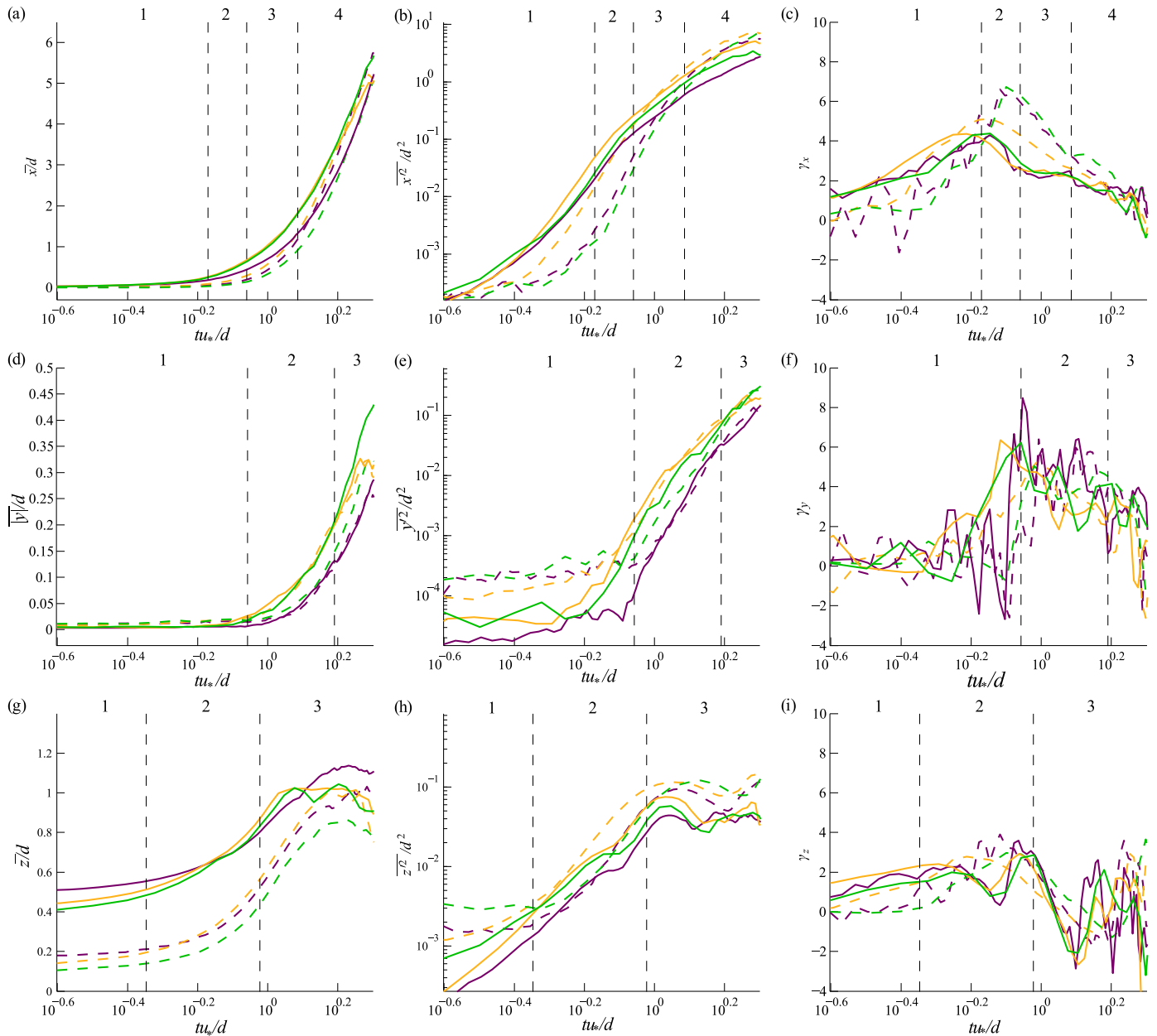


Figure 6 Ensemble-averaged motion from entrainment: (a) streamwise displacement, (b) streamwise diffusion, (c) streamwise diffusion exponent, (d) transverse displacement, (e) transverse diffusion, (f) transverse diffusion exponent, (g) vertical displacement, (h) vertical diffusion, (i) vertical diffusion exponent. The lines are defined in the legend in Fig. 5. Vertical dashed lines divide the plotted range into regions (numbered at the top) to aid the discussion

particles ($\rho/\rho_w = 1.38$) follow similar trends for all submergences (Fig. 6b). The measured range can be divided into four regions for ease of discussion (defined by broken black lines in the figures). In the first region the entraining particles are rising from their initial position in a pocket within the bed to leave the confines of their bed pocket. Whilst in the bed the vertical position of the particle restricts its streamwise position since the flow pushes the entraining particle against the two bed particles that make up the downstream face of its pocket. During this phase, the diffusion exponent increases steadily from an initial value of around 1.5 to a maximum of approximately 4 (Fig. 6c). This is a

significantly higher diffusion exponent than has previously been reported. However, as discussed in Section 1, previous studies have failed to capture this initial motion from a bed pocket despite the fact that it is an inherent stage of particle entrainment in natural systems. Following this first region, there is a second region where the particle tends to roll over the bed particles immediately downstream before it impacts with the bed and moves into a saltation jump. Whether or not the particle remains in contact with the bed whilst it rolls over the immediately downstream bed particles is unclear. Within this region the diffusion exponent decreases rapidly from its maximum to around

2.3. Once the particles escape the bed pocket they undergo a streamwise acceleration (this acceleration phase covers regions 2 (roll over downstream bed particles) and 3 (first saltation jump) of Fig. 6a). In the third region, which covers the first saltation jump, all three submergences display similar near constant exponents of diffusion γ_x of approximately 2.3 (where constant diffusion exponent appears as a straight section in Fig. 6b and a constant value in Fig. 6c). This region corresponds to the first region of Bialik et al. (2012), in whose simulations the particles began on the bed in a fully exposed position, and it agrees well with their finding $\gamma_x \approx 2.32$ (for bed and entraining particles of equal size). A final region is present where the ensemble-averaged streamwise displacement tends towards a constant velocity (i.e. constant gradient in Fig. 6a). Within this region the streamwise diffusion exponent γ_x gradually decreases. The upper bound of this fourth region is imposed by the limitations of the experimental set-up as some particles travel too far from the entrainment position to be tracked, which results in variation in the ensemble-averaged results.

In contrast, the streamwise diffusion for the lower density particles ($\rho/\rho_w = 1.12$) does not exhibit such clear regions and also demonstrates worse agreement between the submergences. Again, there is no systematic dependence on submergence. The lower density particles start at a significantly lower protrusion than the higher density particles. Therefore, they remain in the confines of their bed pocket for longer, until approximately the end of the second region (Fig. 6a). Following a similar trend to the higher density particles, the diffusion exponent (Fig. 6c) reaches a maximum (of between 5 and 6.5 depending on the submergence) when the entrainment particle leaves the confines of the bed pocket (Fig. 6c). The lower density particles move straight into a saltation jump and accelerate through the third region, tending towards a constant velocity in the fourth region. In the third and fourth regions, the exponent decreases at a fairly constant rate for all three submergences.

Diffusion in the transverse direction from the point of entrainment appears to be independent of the particle density (Fig. 6e). The particles are confined in the transverse direction until after they have completely left the bed pocket and passed through the trough between the two bed particles immediately downstream. This results in only a short time interval between the particles becoming free to move in the transverse direction and the end of the tracking (Fig. 6d). Despite this, all of the conditions appear to exhibit similar exponents. The range of transverse diffusion can be divided into three regions to aid the discussion. In the first region, the majority of particles are confined in the transverse direction by the bed arrangement. The second region shows an acceleration in the ensemble-averaged absolute transverse displacement (Fig. 6d) and exhibits diffusion exponents γ_y between approximately 3 and 5 (Fig. 6f). All conditions show a decrease in diffusion coefficient through the region. The particle velocity tends towards a constant in the third region during which the diffusion exponent γ_y appears to decrease (Fig. 6e). These exponents are significantly greater than those for ballistic diffusion,

and are appreciably greater than the exponent of $\gamma_y \approx 2.04$ reported by Bialik et al. (2012), who also found less identifiable regions in the transverse direction than in the streamwise direction. However, the change of the transverse diffusion coefficients with time is much less regular (Fig. 6f) compared to that of the streamwise diffusion (Fig. 6c). This is due to some entrained particles leaving the tracking window during SPIV because of significant transverse displacement.

Previous studies have only considered diffusion in the horizontal plane. In the present work diffusion in the vertical plane is also studied (Fig. 6h). The motion in the vertical direction can be divided into three regions: the first is a region of only slight vertical motion, the second is a region of positive (upward) vertical acceleration and finally the third is the region where the vertical displacement peaks before declining (Fig. 6g). The diffusion exponent increases gradually in the first region. Within the second region, all the considered conditions show a similar trend: the diffusion increases with increasing time with an exponent γ_z of approximately 2 to 3 (Fig. 6i). However, the increase in diffusion is interrupted by bed impacts, at which time the diffusion exponent drops significantly. In the case of the higher density particle, the diffusion exponent exhibits a small dip at $tu_*/d \approx 10^{-0.1}$ associated with the first bed impact shortly after entrainment. However, the diffusion exponent quickly recovers, and this dip does not appear to affect the overall trend through the second region. Both particle types then experience a significant drop in diffusion within the third region.

It was not possible to identify regions that were coherent across all three directions. The different geometric constraints applied in each direction due to the hexagonal close packing arrangement may be responsible for decoupling the diffusion behaviour in the three directions. An integral consideration of the particle motion in all three directions will be covered in Section 4.

3.3 Particle diffusion from the point of collision

Diffusion calculations were also completed with the starting point for each entrainment case set to its first impact with the bed (Fig. 7). This resulted in the streamwise diffusion data conforming to ballistic diffusion (with γ_x varying from 0.85 to 1.07 for the different conditions), as predicted for the local range in Nikora et al. (2001, 2002). Due to the increased travel distance prior to the first impact with the bed, about 20% of the lower density particles did not track to a first impact with the bed and many of those that did were only tracked for a short time after. Therefore, the results presented in Fig. 7 for the lower density particle are shorter in duration and potentially less accurate. Considering only the higher density particles, a similar agreement with ballistic diffusion is seen, with a slight unsystematic variation between submergences (γ_x varying from 1.01 to 1.07). The streamwise diffusion for all cases appears to collapse, with the exception of the low submergence and higher density case with $H = 28.6$ mm and $\rho/\rho_w = 1.38$, which also

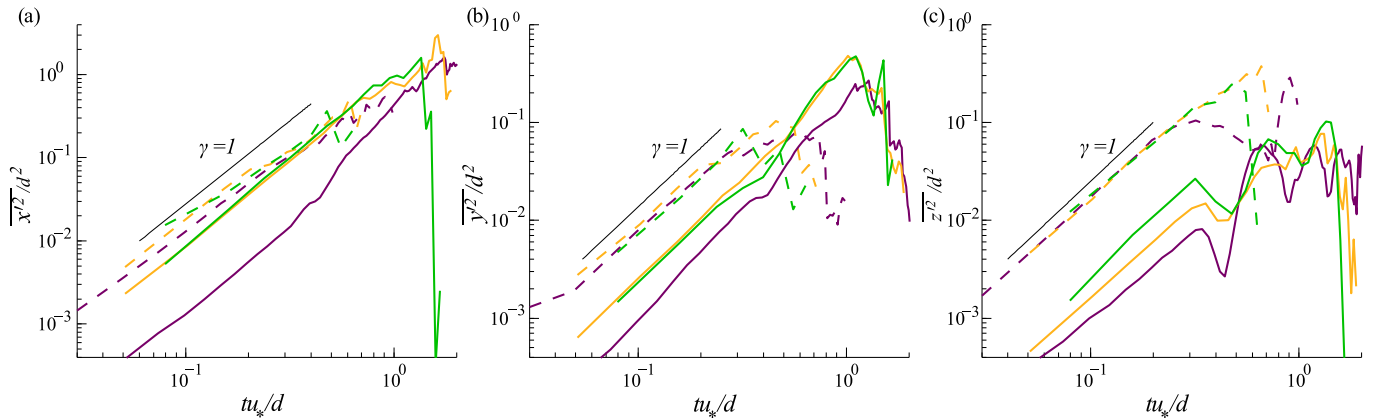


Figure 7 Diffusion from first bed impact: (a) streamwise, (b) transverse, (c) vertical. The lines are defined in the legend in Fig. 5

had a distinctly different ensemble-averaged particle trajectory shape (Fig. 5).

Transverse diffusion from the first impact with the bed resulted in an exponent γ_y varying from 0.93 to 1.15 for the different conditions, which suggests ballistic diffusion in the local range for all cases. Excluding the low submergence higher density case for the reason previously discussed, the transverse diffusion curves from the first bed impact appear to collapse and are independent of submergence but dependent upon the particle density. However, with so few submergences (particularly for the higher density particle) and no concrete reason for the exclusion, this can only be considered as an indication.

Vertical diffusion starting from a bed impact (Fig. 7c) displays an exponent γ_z varying from 0.87 to 1.04 until just prior to a significant decrease, at the time associated with the typical jump duration for each condition. This is very close to the ballistic diffusion experienced in both axes of the horizontal plane within the local region. Vertical diffusion from an impact with the bed for the lower density particles appears to be independent of submergence. In contrast, for the same flow conditions, the higher density particles suggest a dependence on submergence. There is also a distinct separation between the diffusion associated with the different particle densities.

4 Discussion and conclusions

A useful framework for the phases of bedload particle motion is provided by Campagnol et al. (2015). This study complements the work of Campagnol et al. (2015) by providing specific details on the particle acceleration phase. The results presented are limited to a single entrainment event which, with the selected particle densities, results in a relative protrusion range of $0.10 \leq P/d \leq 0.49$. Based on the results presented in the previous sections, here we propose a conceptual model of ensemble-averaged particle trajectory and diffusion at the local scale from the point of entrainment (Fig. 8). There was no clear systematic effect on the relative diffusion as a result

of changing either the submergence or protrusion of the particle. Therefore, these parameters are not accounted for in the model.

The point of entrainment is defined as the first upward motion that leads directly to entrainment. As such, the upward motion of the particle begins as the entraining particle rises out of its bed pocket, making it able to begin to move in the streamwise direction. Whilst rising, the flow pushes the particle against the downstream edge of the bed pocket. In the hexagonal close packing arrangement used in this work, the particle was unable to move in the transverse direction until it had completely left the bed pocket and passed through the trough created by the two immediately downstream bed particles. Due to this, displacement occurs in the streamwise direction before the transverse direction. The particle initially accelerates in the vertical direction before decelerating as it reaches the peak of the saltation jump. In the streamwise and transverse directions the particle accelerates (once free to move) and then tends towards a constant velocity. The different constraints applied to the three coordinate directions are unique to the packing arrangement chosen during this study. However, specific packing arrangements (both uniform and random) will provide different constraints in the three coordinate directions and are therefore likely to diversify the results, as seen in this study. In the more realistic case of a random bed packing with variable grain size and shape, each individual bed particle will have a unique set of constraints. Nevertheless, the overall picture of restraining effects will be similar for different particle arrangements, sizes and shapes. It seems that a proper account of this statistical variability can emerge through additional averaging covering an ensemble of different arrangement scenarios.

The specific motion regions presented in the diffusion for the three coordinate directions do not coincide because of differing geometric constraints in each direction. In both directions in the horizontal plane (streamwise and transverse), the exponent of particle diffusion increases from entrainment and peaks (with an exponent significantly greater than that of ballistic diffusion) as first noticeable displacement occurs in that direction.

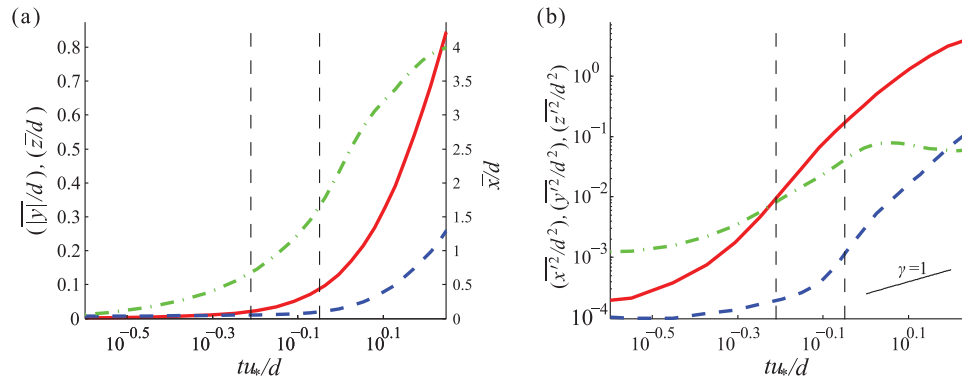


Figure 8 Conceptual model of motion from entrainment at the local scale: (a) displacement, (b) diffusion. The over-bar indicates that the motion is ensemble-averaged across several entrainment events. Solid: streamwise; dash: transverse; dot dash: vertical

The maximum exponent of particle diffusion occurs at the inflection point (indicated by the broken vertical black lines in Fig. 8). The exponent of diffusion then decreases (but remains greater than that of ballistic diffusion) as time increases and it does not reach a stable value within the time frame considered. Further work should track the particle for longer to clarify what, if any, stable value is achieved for the exponent of diffusion as time from entrainment increases.

The results clearly demonstrate the need to separate diffusion from entrainment and diffusion from a random bed contact. Diffusion from the point of entrainment produces exponents significantly greater than that of ballistic diffusion ($\gamma = 1$) in all three coordinate directions. Diffusion from a bed impact, however, demonstrates near ballistic diffusion in all three directions, confirming the prediction of Nikora et al. (2002) and in agreement with the previous studies (e.g. Furbish et al., 2012; Roseberry et al., 2012). This study presents such data for the first time and provides a benchmark dataset for testing computational models (such as the work of Bialik et al., 2015). Further work in this area must clearly define the aspect of the local range being considered, depending on the initial condition of the particle. The work of Bialik et al. (2012) indicates that diffusion from entrainment will tend towards ballistic diffusion if sufficiently long recordings are available. However, these results are based on simulations where the starting point for each entrainment was a fully exposed particle. Therefore, additional work is required to confirm this suggestion.

Acknowledgments

The authors thank the Editor, Associate Editor, Professor F. Balio and two anonymous reviewers for very useful comments and suggestions that helped to improve the final version of the paper.

Funding

The reported work was partly supported by Engineering and Physical Sciences Research Council [EPSRC(UK)], Grant EP/G056404/1 “High resolution numerical and experimental

studies of turbulence-induced sediment erosion and near-bed transport” and Grant EP/K041088/1 “Bed friction in rough-bed free-surface flows: a theoretical framework, roughness regimes, and quantification”.

Notation

d	= particle diameter (m)
f	= PIV sampling frequency (Hz)
F	= Froude number (–)
g	= gravity acceleration (m s^{-2})
G	= image gradient field (–)
H	= flow depth (m)
P	= protrusion (m)
R	= Reynolds number (–)
t	= waiting time (s)
U_b	= bulk velocity (m s^{-1})
u_*	= shear velocity (m s^{-1})
x	= particle position (m)
γ	= diffusion exponent (–)
θ	= image gradient direction (–)
θ_s	= Shields number (–)
ν	= kinematic viscosity ($\text{m}^2 \text{s}^{-1}$)
ρ	= density (kg m^{-3})

ORCID

Vladimir Nikora  <http://orcid.org/0000-0003-1241-2371>

References

- Ahn, S. J., Rauh, W., & Warnecke, H. -J. (2001). Least-squares orthogonal distances fitting of circle, sphere, ellipse, hyperbola, and parabola. *Pattern Recognition*, 34(12), 2283–2303.
- Balio, F., Campagnol, J., Nikora, V., & Radice, A. (2013). Diffusive properties of bed load moving sediments at short time scales. In *Proceedings of 2103 IAHR world congress*, Chengdu, China.

- Bialik, R. J., Nikora, V. I., Karpiński, M., & Rowiński, P. M. (2015). Diffusion of bedload particles in open-channel flows: Distribution of travel times and second-order statistics of particle trajectories. *Environmental Fluid Mechanics*, 15(6), 1281–1292.
- Bialik, R. J., Nikora, V. I., & Rowiński, P. M. (2012). 3D Lagrangian modelling of saltating particles diffusion in turbulent water flow. *Acta Geophysica*, 60(6), 1639–1660.
- Cameron, S. M. (2006). *Near-boundary flow structure and particle entrainment* (Unpublished doctoral dissertation). The University of Auckland.
- Campagnol, J., Radice, A., Ballio, F., & Nikora, V. (2015). Particle motion and diffusion at weak bed load: Accounting for unsteadiness effects of entrainment and disentrainment. *Journal of Hydraulic Research*, 53(5), 633–648.
- Canny, J. (1986). A computational approach to edge detection. *IEEE Transactions on Pattern Analysis and Machine Intelligence*, 8(6), 679–698.
- Drake, T. G., Shreve, R. L., Dietrich, W. E., Whiting, P. J., & Leopold, L. B. (1988). Bedload transport of fine gravel observed by motion-picture photography. *Journal of Fluid Mechanics*, 192, 193–217.
- Fan, N., Singh, A., Fofoula-Georgiou, E., & Wu, B. (2013). Anomalous diffusion for bed load transport with a physically-based model. *AGU Fall Meeting Abstracts*, 1, 1083.
- Furbish, D. J., Ball, A. E., & Schmeeckle, M. W. (2012). A probabilistic description of the bed load sediment flux: 4. Fickian diffusion at low transport rates. *Journal of Geophysical Research*, 117, F03034.
- Martin, R. L., Jerolmack, D. J., & Schumer, R. (2012). The physical basis for anomalous diffusion in bed load transport. *Journal of Geophysical Research*, 117, F01018.
- Nikora, V., Habersack, H., Huber, T., & McEwan, I. (2002). On bed particle diffusion in gravel bed flows under weak bed load transport. *Water Resources Research*, 38(6), 1081.
- Nikora, V., Heald, J., Goring, D., & McEwan, I. (2001). Diffusion of saltating particles in unidirectional water flow over a rough granular bed. *Journal of Physics A: Mathematical and General*, 34(50), L743–L749.
- Nikora, V., McEwan, I., McLean, S., Coleman, S., Pokrajac, D., & Walters, R. (2007). Double-averaging concept for rough-bed open-channel and overland flows: Theoretical background. *Journal of Hydraulic Engineering*, 133(8), 873–883.
- Prasad, A. K. (2000). Stereoscopic particle image velocimetry. *Experiments in Fluids*, 29(2), 103–116.
- Roseberry, J. C., Schmeeckle, M. W., & Furbish, D. J. (2012). A probabilistic description of the bed load sediment flux: 2. Particle activity and motions. *Journal of Geophysical Research*, 117, F03032.
- Witz, M. J. (2015). *Mechanics of particle entrainment in turbulent open-channel flows* (Unpublished doctoral dissertation). University of Aberdeen.